university of groningen / faculty of science and engineering

Rescattering corrections for measurements of neutron cross sections

Bachelor Research Project

Applied Physics

Author:

- Niels de Haan (s4508017)

Supervisors:

- prof. dr. N. Kalantar-Nayestanaki
- prof. G. (George) Palasantzas

July 23, 2024

Abstract

The primary goal of this research is to develop and test a multiple neutron scattering correction factor in Geant4, applied to neutron scattering cross-section measurements from the ELISA setup at GELINA. Disc-shaped carbon targets of thicknesses of 2 mm and 10 mm are placed in a spin-unpolarized neutron beam (ranging from 1 to 8 MeV). This work replicates similar experimental research at the ELISA setup, Joint Research Centre, Geel, Belgium. The ELISA setup geometry is recreated in Geant4, and various physics lists are compared and analysed. Eight virtual detector rings replaced the four rows of eight detectors to test neutron detection efficiency improvement. The multiple scattering percentages are determined over the 1-8 MeV neutron-energy range, for each of the eight detector rings. Finally, the correction factors are computed and implemented on experimentally obtained neutron scattering cross section data from the ELISA setup. Overall, the High Precision neutron model proved to be crucial for obtaining accurate data. A drastic improvement of 700% on neutron detection efficiency was found subsequent to implementing the new detector configuration. Also, the correction factor showed to be improving the deviations for detector angles farther away from 90° and inaccurate for measurements done by detectors placed close to 90°.

Contents

1 Introduction

In this study, the aim is to obtain a correction factor that accounts for the multiple scattered neutrons in the total neutron yield. The number of scattering events that hit a nearby detector depends on the size of the sample, as deviations were found in experiments with similar sample sizes and incident neutron energies [1]. This is an important observation, because the understanding of the multiple scattering interactions between neutrons and nuclei is still not described very accurately in nuclear models [2]. When a neutron interacts with a sample carbon nucleus, it can cause a wide range of events, including neutron-capture and more interestingly, within the 1-8 MeV energy range, multiple scattering of neutrons. In the case of this neutron multiple scattering, the process is analysed by detecting neutrons scattered by carbon using an array of 32 High Purity Germanium (HPGe) detectors arranged around the sample [1] [3]. This particular study is performed using the Geant4 toolkit which is made for simulating the passage of particles (such as high energy neutrons) through matter. The simulations represent the environment at the GELINA (Geel Electron LINear Accelerator) facility in Geel, Belgium. By reproducing this experimental environment, combined with the necessary physics toolkits provided by Geant4, a representation of reality can be simulated and analysed. Monte Carlo methods are critical in this context as they enable statistical modelling of complex physical processes in situations such as describing and predicting neutron scattering events. Geant4 is a software tool that uses Monte Carlo simulations. Therefore, with Geant4, a correction factor for various sample sizes and neutron energy may be calculated. After implementing this correction on experimental neutron scattering cross section data for 2 mm and 10 mm thick carbon targets, they should yield the same results, therefore removing the target geometry and thickness influence on the cross sections. The incompleteness of current nuclear physics models makes neutron-nucleus interactions important to study experimentally. These models frequently struggle to adequately characterise such phenomena due to the numerous variables and interactions involved [4]. By improving these models, physicists can gain a better understanding of (elastic) interactions between nucleons and nuclei. The data analysis is performed using Python.

The objective of this simulation study is to find a reliable correction factor at a variety of incident neutron energies (1-8 MeV) that successfully removes the impact of target geometry and thickness on the cross section measurements. Several physics lists are tested and analysed using previous research and nuclear databases. For eight angles, the multiple scattering correction factor is calculated and applied to the obtained neutron cross section data. The method that is used for obtaining the correction factor should work on sample materials other than carbon. It helps to produce more accurate predictions for neutron-induced scattering events for numerous materials. More precise nucleon-nucleus interactions prediction-capabilities are critical for a variety of applications, one of which is designing and choosing nuclear reactor materials [5]. Furthermore, by enhancing the accuracy of the predictions that are being made using the current state-of-the-art nuclear models, this research may be of much importance.

2 Theory

2.1 The ELISA setup at GELINA

The ELISA (ELastic and Inelastic Scattering Array) array is used for neutron and gamma ray detection at the GELINA (Geel Electron LINear Accelerator) facility [6]. In order to create the neutron beam, an electron beam is accelerated by the GELINA accelerator and directed at a uranium target. Upon striking the uranium target, the electrons induce bremsstrahlung, which produces high energy photons. The produced photon collides with a uranium nucleus, exciting it. As a result, the uranium nucleus emits a neutron. These neutrons are directed towards the carbon scattering target through the use of collimators, resulting in a spin-unpolarized neutron beam. Subsequent to colliding with the carbon target, the neutrons may scatter zero, once or multiple times off the target sample nuclei, after which the neutrons are detected by one of the surrounding detectors.

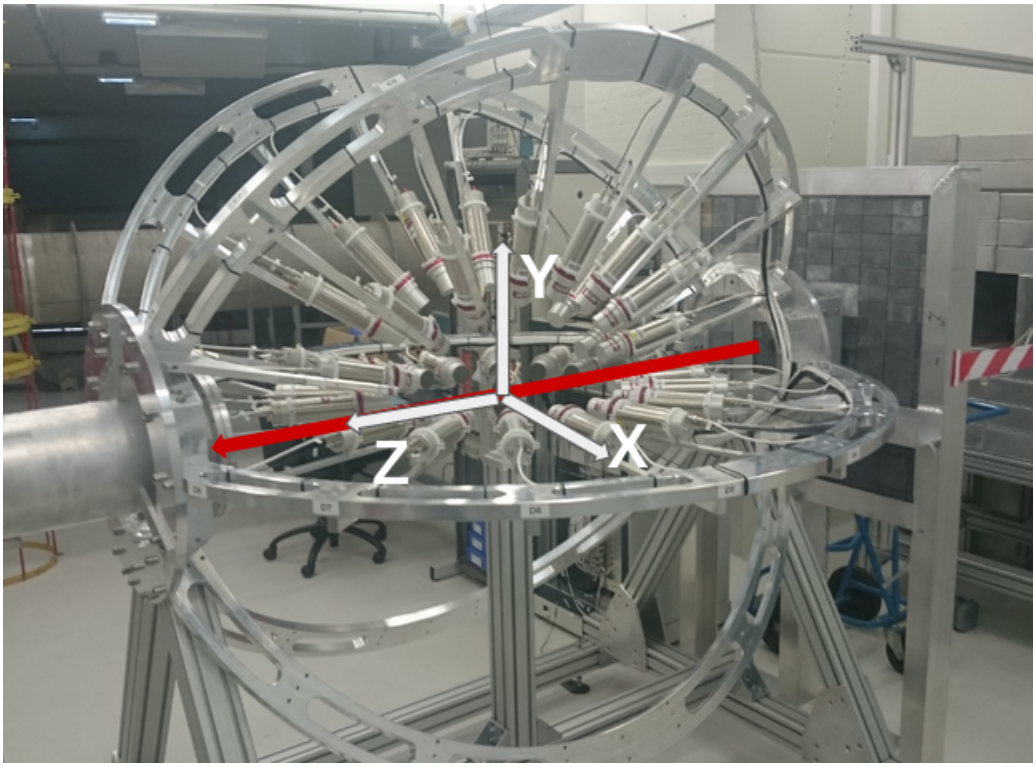

Figure 1: Picture of the ELISA setup. The 32 detectors are placed in four rows of eight detectors around the carbon target [3]. The coordinate system depicted in the image is used as a reference throughout the report.

The neutron detector setup of the ELISA experimental setup is composed of 32 liquid organic scintillation detectors, as shown in figure 1. Half of the 32 detectors are the EJ-301 liquid scintillator type, while the other half are the EJ-315 type [7] [8]. The four rows of detectors are placed at four specific angles, these azimuthal angles are; -90°, -30°, 30° and 90° (see figure 1 for coordinate system defini-

tion). At each of those azimuthal angles, there is a row of eight detectors placed at the following polar angles; 16.2°, 37.2°, 58.3°, 79.2°, 100.6°, 121.7°, 142.8° and 163.8° [3]. The mentioned detector angles are displayed in Figure 2 below.

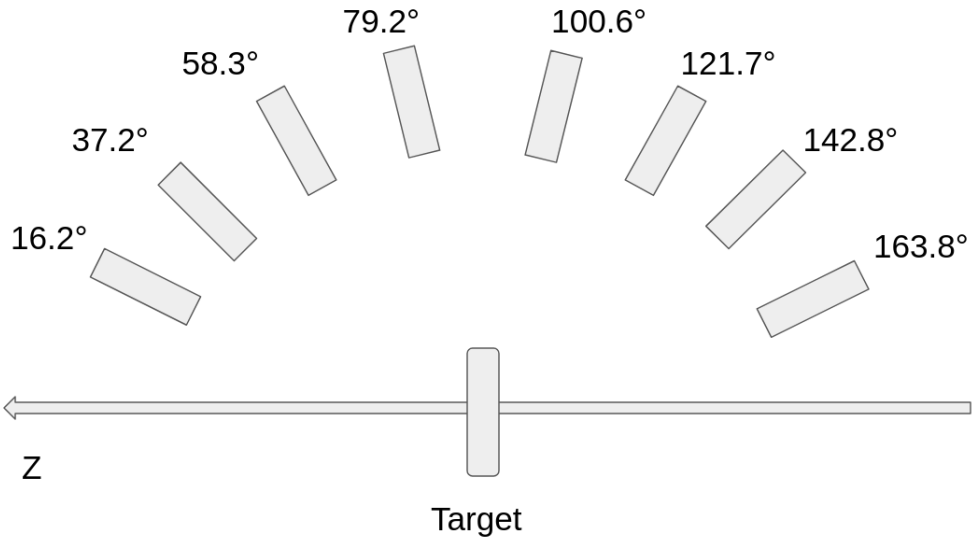

Figure 2: Schematic of the detector setup, consisting of the carbon target in the center with the eight detectors placed around it. Each of the detectors is placed at a distinct polar angle.

2.2 Time-of-flight

The time-of-flight is defined as the time it takes for the incident neutron to travel from the source to the target. Deriving the time-of-flight equation requires the energy-mass relation,

$$E = \gamma mc^2, \tag{1}$$

where E is the total energy of the neutron, m is the neutron mass, c is the speed of light in a vacuum and γ is the Lorentz factor, which is defined as

$$\gamma = \frac{1}{\sqrt{1-\frac{v^2}{c^2}}}, \tag{2}$$

where v is the relative velocity between the neutron and the laboratory frame. The incident neutron energy E_0 is defined as the difference between the total neutron energy E and the rest energy E_R, where $\gamma = 1$ as the neutron is stationary, resulting in

$$E_0 = mc^2 \left(\frac{1}{\sqrt{1-\frac{v_0^2}{c^2}}} - 1 \right). \tag{3}$$

From equation 3, the neutron time of flight is obtained,

$$t.o.f = \frac{d}{c\sqrt{1-1/(1+\frac{E_0}{mc^2})^2}}, \tag{4}$$

where d is the distance from the neutron source to the target. Since the neutron energy does not exceed 8 MeV, the highest neutron velocity is $3.91 * 10^6 m/s$, which results in $\gamma \simeq 1.008$. So $\gamma < 1.008$ for the 1-8 MeV neutron energy range, which indicates that the relativistic effects at this energy range are negligible. Therefore, the time-of-flight is estimated using

$$E_k = \frac{1}{2}mv_0^2, \tag{5}$$

which results in

$$t.o.f = d\sqrt{\frac{m}{2E_0}}. \tag{6}$$

2.3 Neutron scattering

When accelerated neutrons interact with a nucleus, a wide range of reactions can take place. In the fast-neutron energy range (1-20 MeV), the most prominent reaction is neutron scattering. When a fast neutron interacts with a carbon nucleus, the neutron scatters of the nucleus, see figure 3 below.

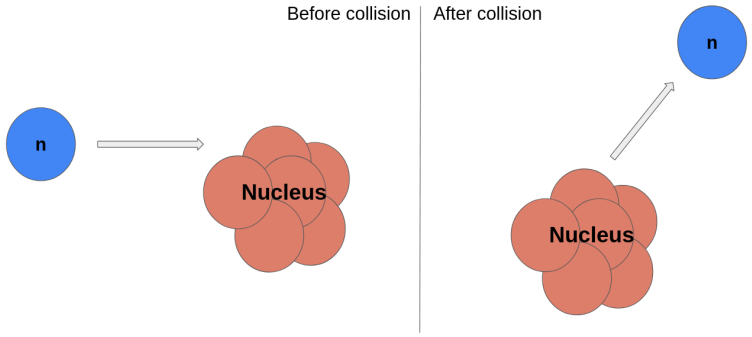

Figure 3: Schematic of a neutron scattering event, where an incident neutron scatters off a target nucleus.

Within this reaction type, two distinguishable variants occur. The first is neutron elastic scattering, which is the most occurring reaction for carbon in the fast-neutron energy range [9]. When a neutron scatters elastically from a nucleus, it conserves most of its kinetic energy. Some energy is transferred from the neutron to the nucleus during an elastic neutron scattering event, but not enough to excite a nucleus of the target. This relatively small energy exchange is what causes the target nuclei to recoil shortly after the collision event. For neutron energies above 4.5 MeV, inelastic scattering starts to occur. During an inelastic neutron scattering event, the neutron transfers a fraction of its energy to the

nucleus. This results in a decrease in kinetic energy subsequent to colliding with the nucleus. Above the 4.5 MeV inelastic neutron inelastic scattering threshold (within the fast-neutron energy range), elastic scattering remains the most probable reaction, followed by inelastic neutron scattering [9].

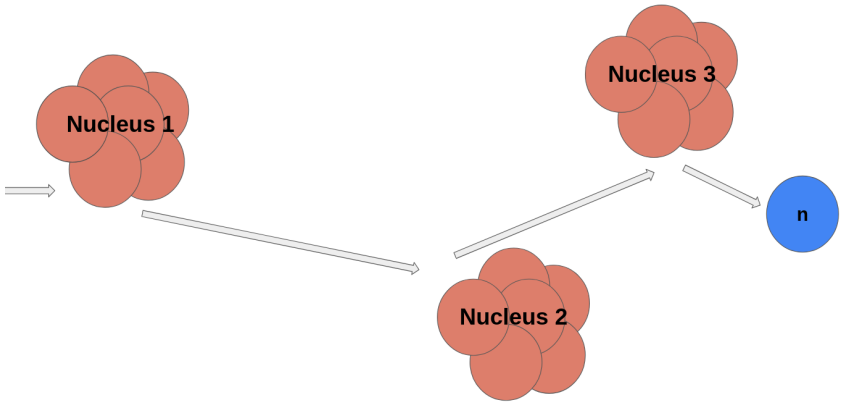

Figure 4: Schematic of a neutron multiple scattering event, showcasing a scenario where the incident neutron scatters of three target nuclei (indicated by 1,2 and 3).

As the target samples consist of enormous numbers of nuclei (exceeding 10^{23} nuclei for a 1 cm^3 target sample), it is likely that a scattered neutron interacts with more than one target nucleus. This phenomenon is called multiple scattering, as depicted in figure 4. In the next sub-chapter, the percentage of scattered neutrons that show multiple scattering is explained in further detail.

2.4 Multiple scattering percentage and error analysis

The multiple scattering percentage (MSP) is defined as the percentage of neutrons that have scattered more than once prior to entering a detector volume over the total number of neutrons that enter a detector.

$$MSP = \frac{C_{>1}}{C_T} * 100\%. \tag{7}$$

The corrected neutron scattering cross sections for each separate detector over the entire energy range are computed using

$$\sigma_{cor}(E, det) = (1 - MSP/100)\sigma_{scatt}. \tag{8}$$

All neutron detection events in the detector volumes are independent of each other, therefore, the errors in the neutron yield can be described by the Poisson distribution. Therefore, the standard deviation of the neutron yield σ_{Poisson} are described by:

$$\sigma_{Poisson} = \sqrt{C}, \tag{9}$$

where C represents the number of counts for each detector. From this distribution, the following standard deviations can be deduced,

$$\Delta C_{>1} = \sqrt{C_{>1}}, \qquad \Delta C_T = \sqrt{C_T}, \tag{10}$$

where $C_{>1}$ is the total number of counts (neutrons) in a detector with more than one scattering event and T is the total number of counts in a detector. As the multiple scattering percentage is dependent on two stochastic variables, the errors in both counts should be taken into consideration. The absolute error is derived from the partial derivative error formula given by

$$\Delta MSP = \sqrt{\left(\frac{\partial MSP}{\partial C_{>1}}\right)^2 (\delta C_{>1})^2 + \left(\frac{\partial MSP}{\partial C_T}\right)^2 (\delta C_T)^2 + 2\left(\frac{\partial MSP}{\partial C_{>1}}\right)\left(\frac{\partial MSP}{\partial C_T}\right) Cov(C_{>1}, C_T)}, \tag{11}$$

resulting in

$$\Delta MSP = 100\sqrt{\frac{C_{>1}}{C_T^2} - \frac{C_{>1}^2}{C_T^3}} \tag{12}$$

Finally, the relative error of the multiple scattering percentage is described by

$$\frac{\Delta MSP}{|MSP|} = \sqrt{\frac{1}{C_{>1}} - \frac{1}{C_T}} \tag{13}$$

Derivations of the formulas used for the error analysis can be found in the Appendix.

3 Methods

3.1 Geant4 construction

The first step in this project is to create a virtual model of the ELISA setup . The code is constructed in such a way that it closely represents the most important facets of the experimental setup at GELINA; the monochromatic neutron beam, the cylindrical carbon target and the placement and distribution of the neutron detectors. First, let us describe the software that is used. Geant4 (GEometry ANd Tracking) is developed as a multi-functional physics tool that is used for simulating the interactions and passage of radiation through matter [10]. The 32 detectors are placed along eight polar angles around the neutron beam axis. The angles are listed in table 7.1 in the Appendix. The distance between the target and each detector is 29.5 cm, as in the experimental setup [3]. centred inside the virtual box is the cylindrically-shaped carbon target. The average isotopic abundance of carbon in its natural form on earth is 98.89% ^{12}C and 1.11% ^{13}C, which is therefore the chosen composition of the carbon target in the simulation [11]. In figures 21 and 22, the cross sections for elastic and inelastic scattering can be observed for the 1-8 MeV neutron energy range. The radius of the carbon target is 5 cm and the thicknesses of 2 mm and 10 mm are analysed and compared after processing the data.

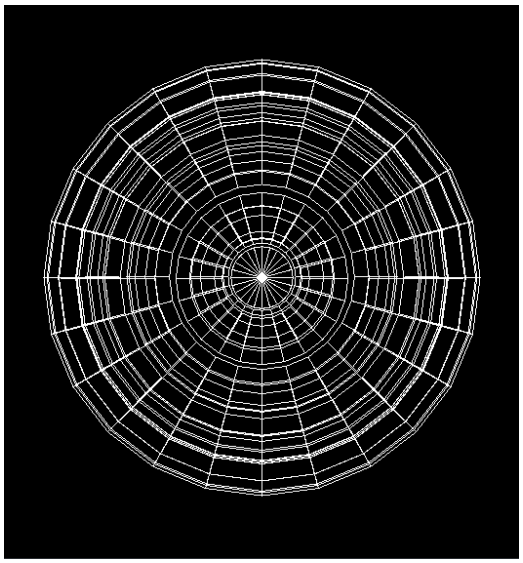

(a) Front view of the created ELISA setup in Geant4 for simulation of the scattered neutrons. From this orientation, the neutrons propagate out of the page.

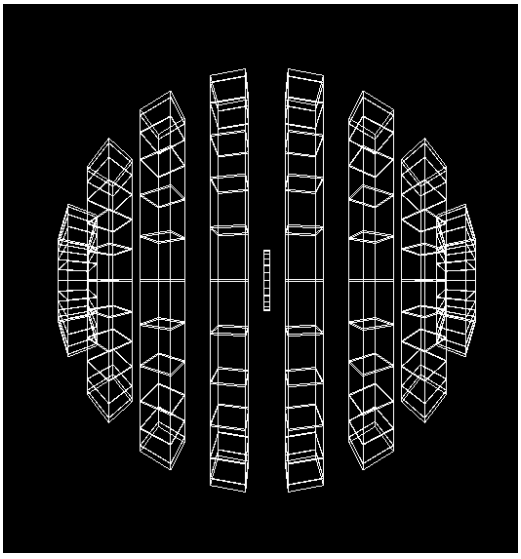

(b) Side view of the ELISA setup in Geant4. The neutron beam enters from the left side. Notice the target in the centre of the spherically arranged detectors.

Figure 5: ELISA setup in Geant4: Front view (a) and Side view (b).

The initial construction of the ELISA setup in Geant4 consisted of 32 detectors, like in the experimental setup. In order to increase efficiency of the setup, the 32 detectors were replaced by 8 detector rings. This does not affect the distribution of neutrons over the eight detectors, since the differential

neutron cross section is, for unpolarized neutrons, independent of azimuthal angles. The eight rings were placed around the same polar angles, found in table 7.1, as the detectors in the setup at GELINA.

3.2 Physics lists and Assessment

Geant4 uses physics lists that are responsible for describing the particle type and the physics processes associated with each particle type. Depending on the application of the project, the correct physics lists should be incorporated in the Geant4 simulation. Physics lists are incorporated in Geant4 for a wide range of particle processes, such as elastic and inelastic neutron interactions. For that, the models used for calculations in the simulation use a variety of databases and assumptions. In the following paragraphs, descriptions are given for each of the tested models. The testing method consists of analysing the increase in the percentage of scattered neutrons that scatter more than once in the carbon target subsequent to entering a detector volume. In Geant4, one has to select a high-energy physics list (Quark-Gluon String model or Fritiof Parton model) together with a low-energy physics list (Bertini Cascade model or Binary Cascade model) and, optionally, together with the High Precision Neutron model. To illustrate, this is how a physics list is Incorporated in Geant4: `G4HadronPhysicsQGSP_BERT_HP` (Quark-Gluon String model, Bertini Cascade model and High Precision Neutron model) or `G4HadronPhysicsFTFP_BIC` (Fritof Parton model and Binary Cascade model). For some angles, at a neutron energy of 4.5 MeV, the multiple scattering percentage increases drastically due to inelastic scattering becoming more apparent than elastic scattering [1].

The Fritiof Parton model (FPF) uses a unique method for describing hadronic particles, such as neutrons [12]. It assumes that hadrons can be treated as a collection of point-like sub-particles. We can interpret this as a relativistic addition to the quark model, as quarks appear to form a continuum of partons at high-energies. As these relativistic effects are relevant only at high energies (> 5 GeV), this model requires additional modifications for it to function well at lower energies (< 10 MeV). The next model that is tested is the Quark-Gluon String model (QGS) [13]. This model uses the concept of string excitation between quarks and gluons. For example, when a high energy neutron collides with a nucleus, the components of the colliding particles interact in a complex manner. The quarks and gluons inside the colliding neutron and the nucleus' proton for example, transfer energy upon collision, effectively creating strings of energy that are interconnected between colliding quarks. Interestingly enough, when these strings continue to stretch, moments subsequent to collision, the string essentially breaks into smaller particles. The model is capable of predicting and describing interactions between these particles with great accuracy. The two models that have been described so far have proven to be very effective for the particle interactions above 5 GeV and 15 GeV, respectively. Concluding, the Fritiof Parton and the Quark-Gluon String models handle the initial interaction and production of secondary particles between hadronic particle collisions, but both only work in an energy range far outside the 1-8 MeV range used in this research.

The following two models are cascade models, designed to describe the subsequent interactions be-

tween particles like neutrons and nuclei. Furthermore, these cascade models tend to be more effective at describing particle interactions below 10 GeV. Therefore, the following two models are used and tested in combination with the previous two models, as shown later on in the results. The third model is the Binary Cascade Model (BIC) [14], a model that computes the scattering effects through a binary process, meaning that each nucleon of the incoming beam interacts individually with the nucleons of the target particle. Furthermore, it includes probabilistic calculations used to determine the likelihood of various reactions, such as inelastic neutron scattering. Lastly, it models the behaviour and propagation of the produced particles that were born subsequent to hadronic collisions. The last considered model is the Bertini Intranuclear Cascade Model (BERT) [15]. The intranuclear model has many similarities to the previously mentioned binary model, such as considering the geometry of particles, their cross sections and the modelling of the cascade of produced particles by the reaction. However, this model has a more probabilistic approach of the individual particles during the collision event, making it more sophisticated for more detailed but computationally expensive simulations.

The last model is the high-precision model, used for low neutron energies (¡20 MeV). This model uses neutron scattering databases, such as the ENDF-B/VIII data library, for determining the cross sections and final states for neutron-induced reactions [16]. The data from these databases incorporate probabilities of elastic scattering, inelastic scattering, neutron capture and neutron induced fission. Of these, elastic and inelastic scattering are the main focus points in this research. Excitation of nuclei due to inelastic scattering are taken into account. The excitation of a nucleus can result in a wide range of final states, after interacting with the incident neutron. Once the reaction type for the interaction between the nucleus and the neutron at a specific energy is determined, the model uses the data from the scattering databases to simulate the particles produced by the reaction. The high-precision model is expected to be crucial for the energy range in this research, since it is designed for simulations with neutron energies below 20 MeV.

The assessment of the combinations of these physics lists is done by inspecting the simulated angular neutron distribution for energies between 1 and 8 MeV. The obtained data is reviewed for a drastic increase in the multiple scattering percentage around the inelastic scattering threshold, around 4.5 MeV [16] [17]. The impact of the high-energy models are insignificant, as the energy range of those models (¿5 GeV) exceed the energy range used in this research (1-8 MeV) by a large margin. Therefore, the low-energy models are only relevant for this research. For this research, the Fritiof Parton model, together with the Binary Cascade model and the High Precision neutron model are used. Further results and conclusions regarding testing the individual physics lists combinations are discussed in Chapter 5.

3.3 Neutron detection acceptance

The experimental setup ELISA consists of an arrangement of 32 neutron detectors. As these detectors cover a relatively insignificant area surrounding the carbon target, the 32 detectors are replaced by a total of eight rings and tested for an increase in neutron yield (see figure 6). Initially, the detectors are placed at four discrete azimuthal angles, relative to the neutron beam. Each of the four angles consists of eight detectors placed at discrete polar angles, relative to the neutron beam. The detectors at the discrete azimuthal angles are removed and replaced by a single detector ring, encompassing the entire azimuthal angle of 360°. Finally, the new setup in Geant4, composed of eight detector rings, is tested by summing the total neutron yield of each detector at the 1-8 MeV neutron energy range, with steps of 1 MeV. This method allows for a simple, yet accurate method for calculating the overall improvement in the acceptance for detecting neutrons.

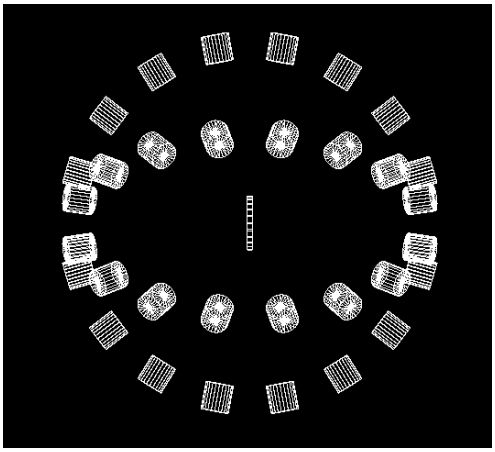

(a) XZ-projection of the replicated setup of ELISA in Geant4. The neutron beam enters from the left side. Notice the target in the centre of the 32 spherically arranged detectors.

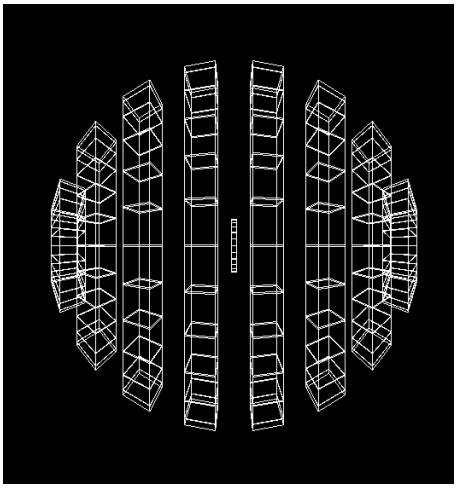

(b) XZ-projection of the to-be tested setup in Geant4. The neutron beam enters from the left side. Notice the target in the centre of the eight spherically arranged ring-shaped detectors.

Figure 6: ELISA setup in Geant4: Initial design (left) and new design (right).

3.4 Multiple scattering correction factor

After determining the most accurate physics list combination, the tests are started for the 1-8 MeV energy range. These are formatted in .ROOT files by Geant4 which, subsequent to reformatting, are used for the data analysis. First, the multiple scattering percentages are calculated using equation 7 and stored in separate arrays. Then, using equation 13, the errors of the multiple scattering percentage are calculated and stored in a similar manner as the previously calculated multiple scattering percentage. These values are then plotted for each of the eight detector rings as a function of energy. In a similar manner, plots are created for the total experimental neutron scattering cross sections as a function of energy. The experimental neutron scattering cross sections are corrected using the calculated multiple scattering correction factor using equation 8. Using this method, the effects that the thickness of the target sample has on the measured neutron scattering cross sections should be corrected for. Therefore, after correcting the experimental neutron scattering cross sections for the 2 mm target and the 10 mm target, both should yield the same results. The deviations between the neutron scattering cross sections are analysed and used for drawing conclusions on the accuracy of the method. The goal is to obtain a deviation between the 2 mm and 10 mm data smaller that 5%.

4 Results

In this chapter, all results required to achieve the research goal are presented with brief explanations. Further results can be found in the Appendix.

4.1 Physics lists

Figure 8 shows the multiple scattering percentage as a function of incident neutron energy for all eight detectors with a target thickness of 10 mm. Plots of the other physics list combinations (figures 23,24 and 25) are located in the Appendix, as all tested combinations yielded identical results.

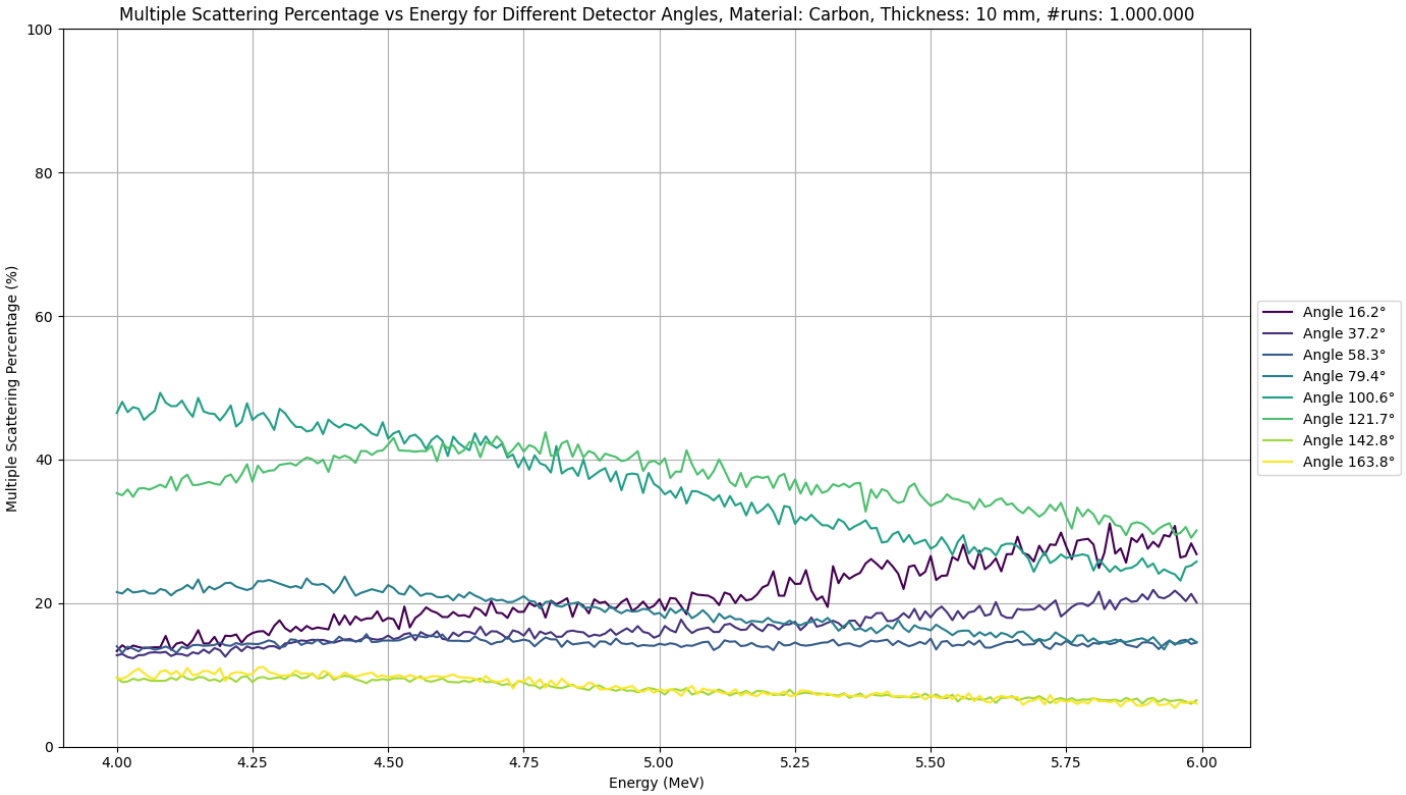

Figure 7: Multiple scattering percentage plot for 4-6 MeV, using the Quark-Gluon String model and the Binary Cascade model.

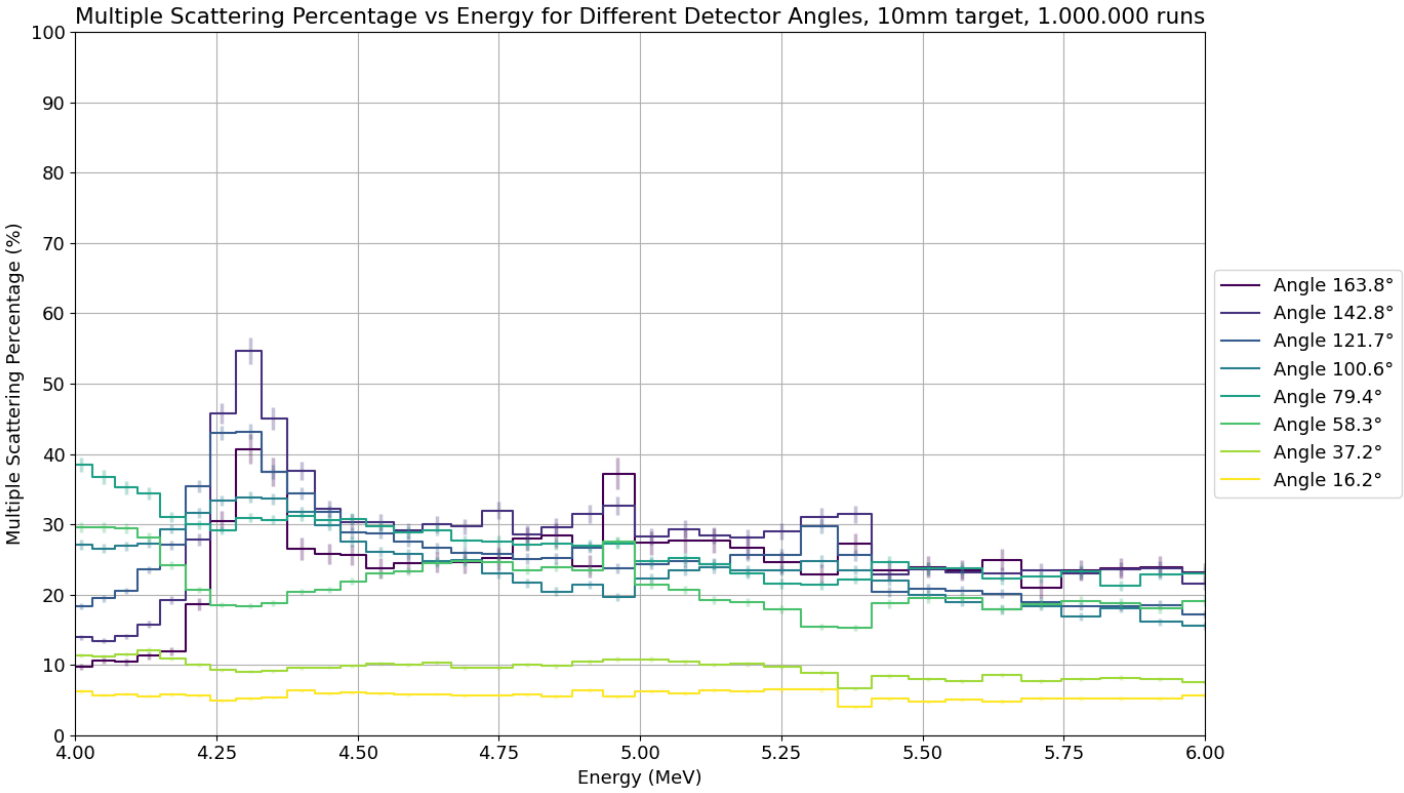

Figure 8: Multiple scattering percentage plot for 4-6 MeV, using the Fritiof Parton, Binary Cascade and the High Precision neutron models.

4.2 Neutron detection efficiency

Figures 9 and 10 depict the total neutron yield of all detectors combined per energy interval for the 2 mm and 10 mm thick targets. In this comparison, the Fritiof Parton, Binary Cascade and the High Precision neutron models are used for simulating the data.

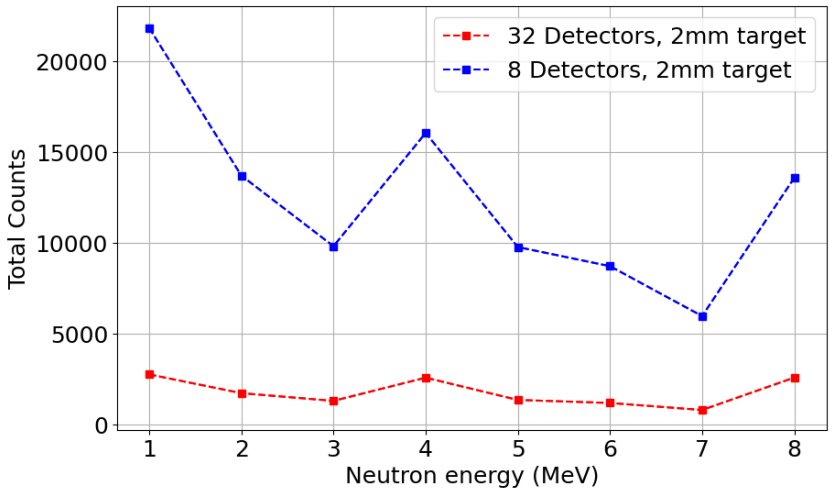

Figure 9: Neutron count for the 2 mm thick target, using the original detector setup and the improved ring-shaped detector setup.

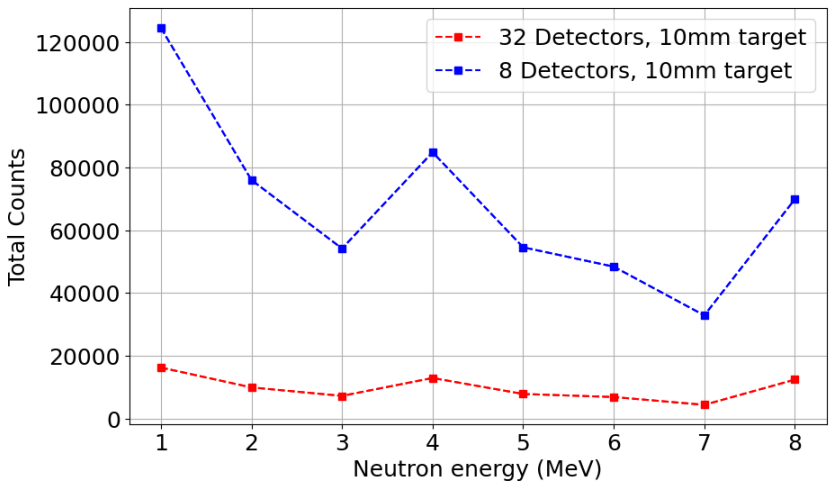

Figure 10: Neutron count for the 10 mm thick target, using the original detector setup and the improved ring-shaped detector setup.

The new ring-shaped detector setup in Geant4 results in an average increase of 700% in total neutron count for the 2 mm and 10 mm targets.

4.3 Multiple scattering percentages

In this section, the multiple scattering percentages calculated using equations 7 are displayed in figures 11 and 12 for the target thicknesses of 2 mm and 10 mm. Notice that the multiple scattering percentages do not exceed $28.2 \pm 2.6\%$ and $70.1 \pm 1.1\%$ at target thicknesses of 2 mm and 10 mm, respectively.

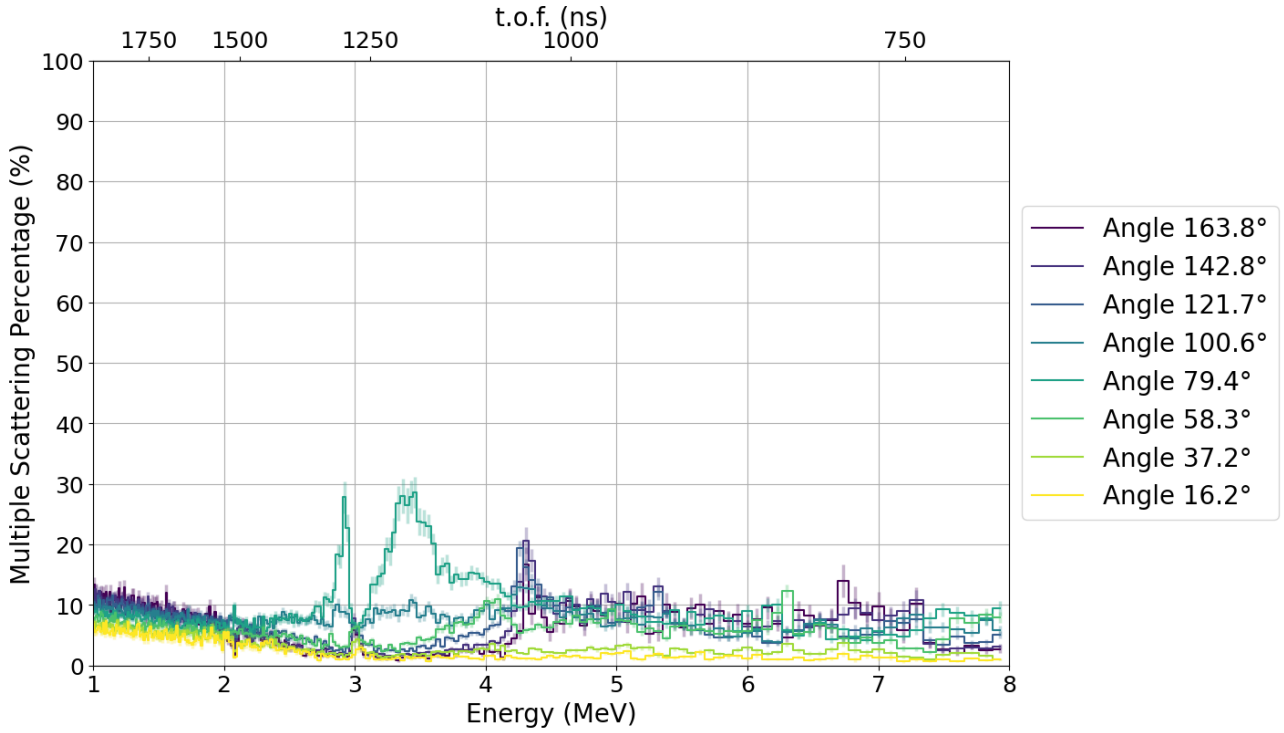

Figure 11: Multiple scattering percentages for the 2 mm thick carbon target, calculated using the data obtained in Geant4.

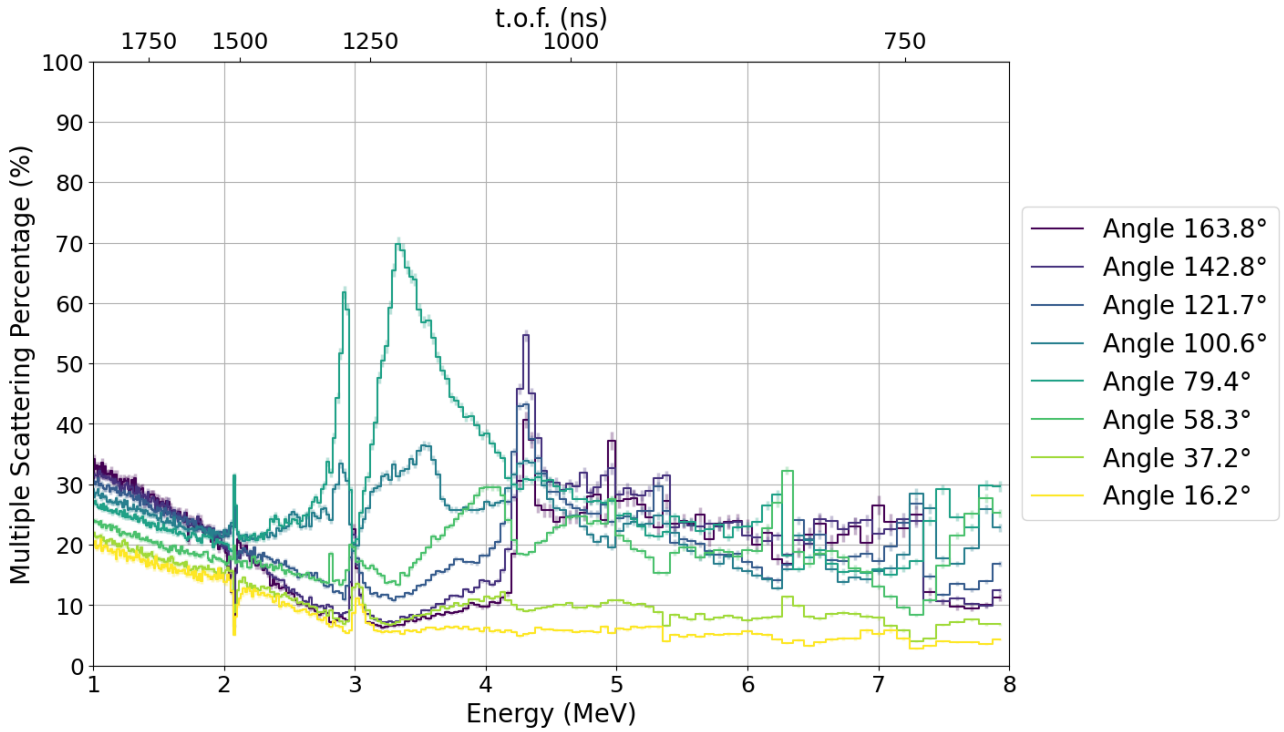

Figure 12: Multiple scattering percentages for the 10 mm thick carbon target, calculated using the data obtained in Geant4.

4.4 Corrected neutron cross sections

The corrected neutron cross section for all eight detectors for the 2 mm and 10 mm thick targets are displayed in this section. The average improvement over the entire energy range (1-8 MeV) for each detector is tabulated in Table 1.

Detector angle	Prior to correction	Subsequent to correction	Improvement
163.8°	16.8%	$10.5 \pm 3.2\%$	$6.3 \pm 2.5\%$
142.8°	16.6%	$8.1 \pm 2.8\%$	$8.5 \pm 2.4\%$
121.7°	13.1%	$9.4 \pm 3.1\%$	$3.7 \pm 2.5\%$
100.6°	9.8%	$24.7 \pm 5.0\%$	$-14.9 \pm 3.2\%$
79.4°	17.8%	$18.6 \pm 4.3\%$	$-0.9 \pm 2.9\%$
58.3°	8.3%	$9.5 \pm 3.1\%$	$-1.2 \pm 2.5\%$
37.2°	8.2%	$6.7 \pm 2.6\%$	$1.5 \pm 2.3\%$
16.2°	11.1%	$6.3 \pm 2.5\%$	$4.8 \pm 2.2\%$

Table 1: Comparison of percentage differences between the 2 mm and 10 mm target prior to and subsequent to correction at various detector angles.

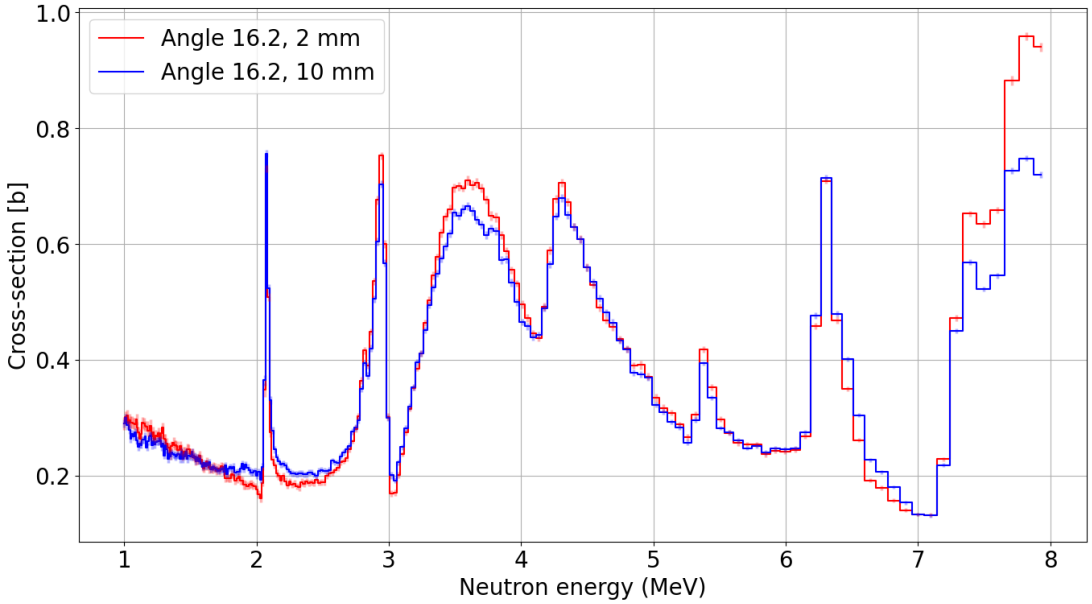

Figure 13: The experimental cross sections for the 2 mm and 10 mm target thicknesses with the correction factors implemented for the detector placed at 16.2°.

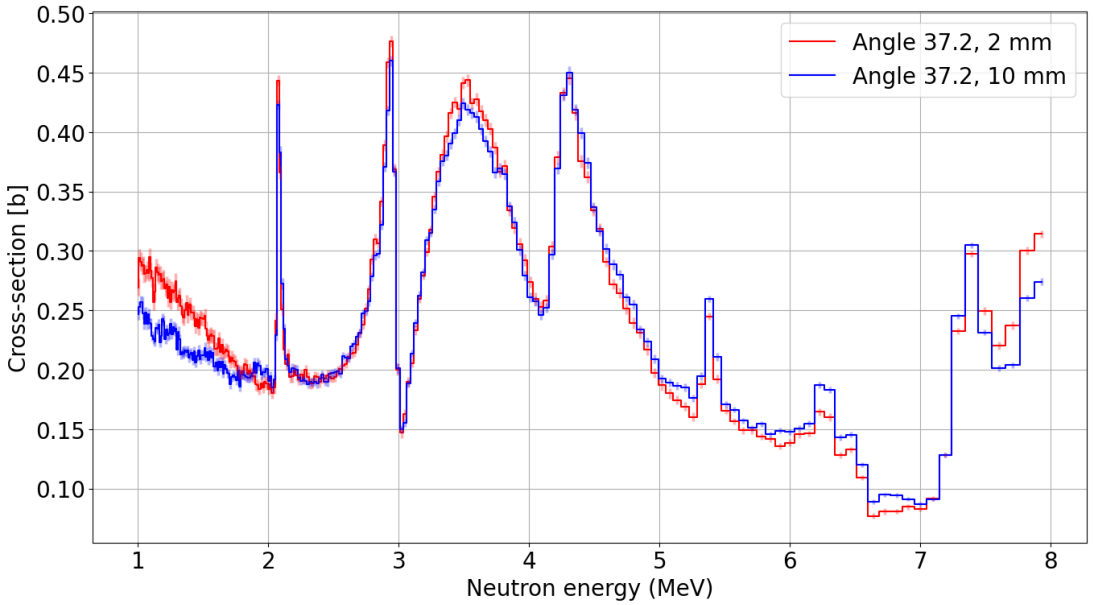

Figure 14: The experimental cross sections for the 2 mm and 10 mm target thicknesses with the correction factors implemented for the detector placed at 37.2°.

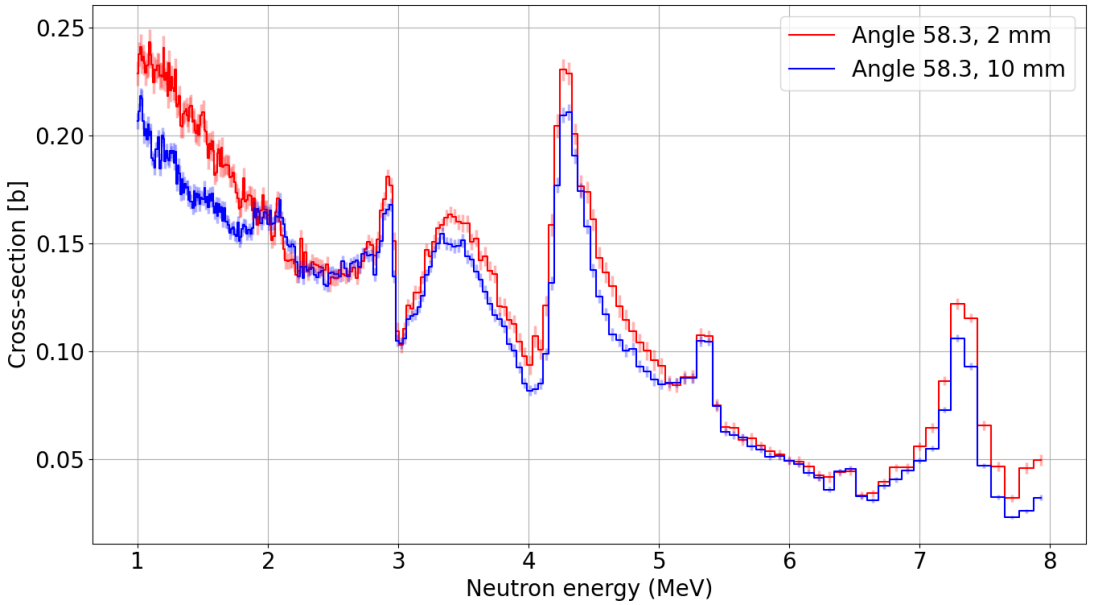

Figure 15: The experimental cross sections for the 2 mm and 10 mm target thicknesses with the correction factors implemented for the detector placed at 58.3°.

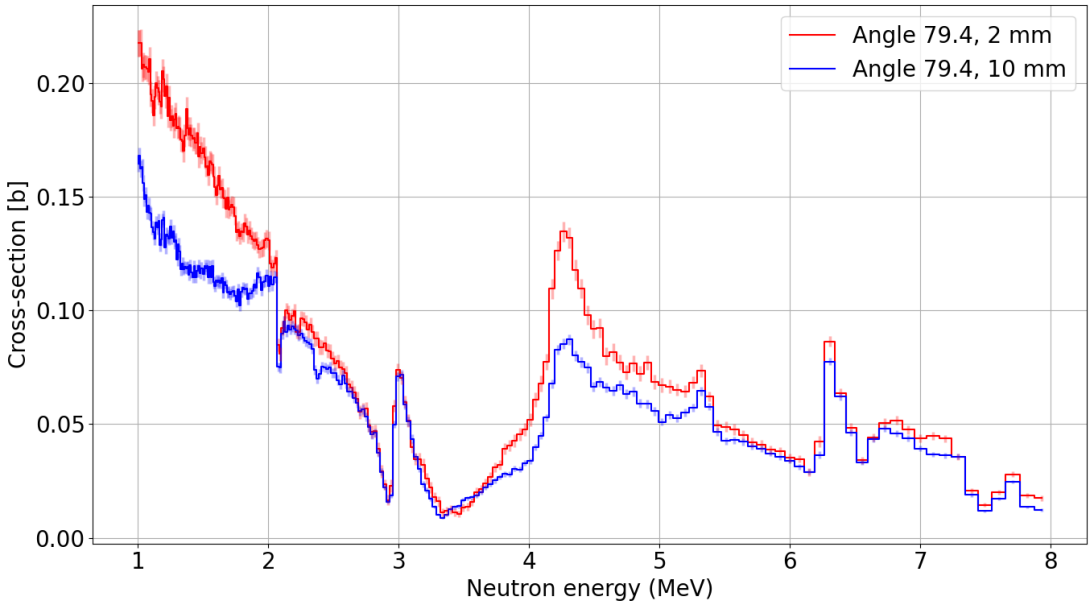

Figure 16: The experimental cross sections for the 2 mm and 10 mm target thicknesses with the correction factors implemented for the detector placed at 79.4°.

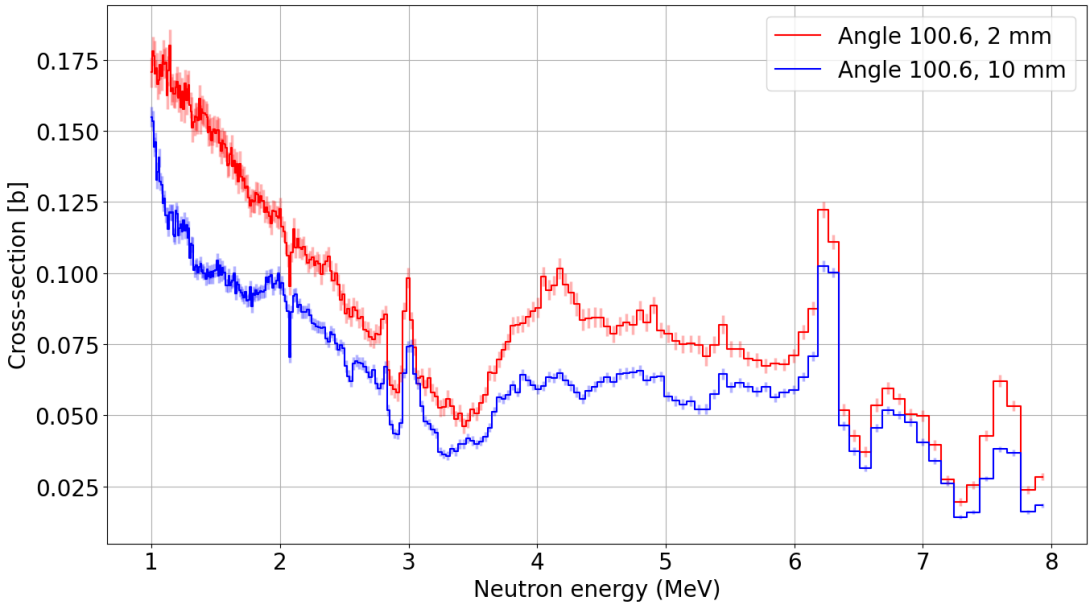

Figure 17: The experimental cross sections for the 2 mm and 10 mm target thicknesses with the correction factors implemented for the detector placed at 100.6°.

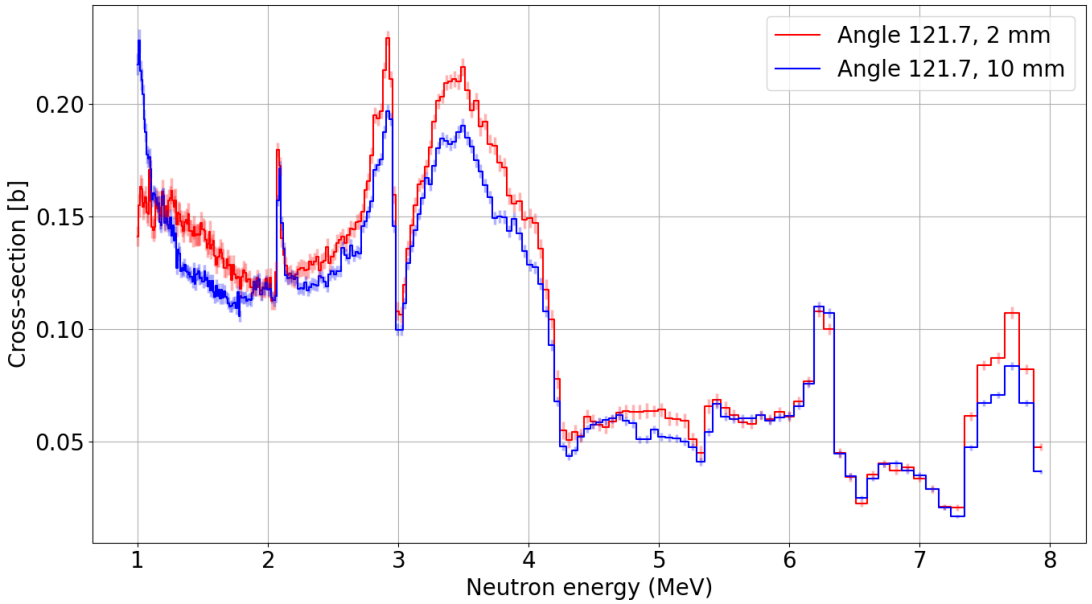

Figure 18: The experimental cross sections for the 2 mm and 10 mm target thicknesses with the correction factors implemented for the detector placed at 121.7°.

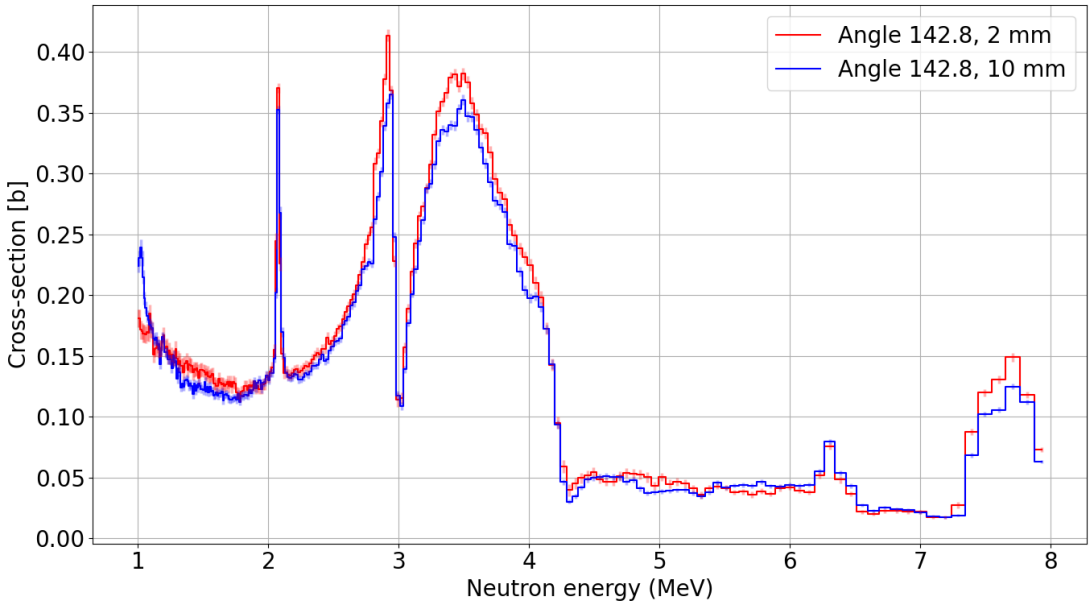

Figure 19: The experimental cross sections for the 2 mm and 10 mm target thicknesses with the correction factors implemented for the detector placed at 142.8°.

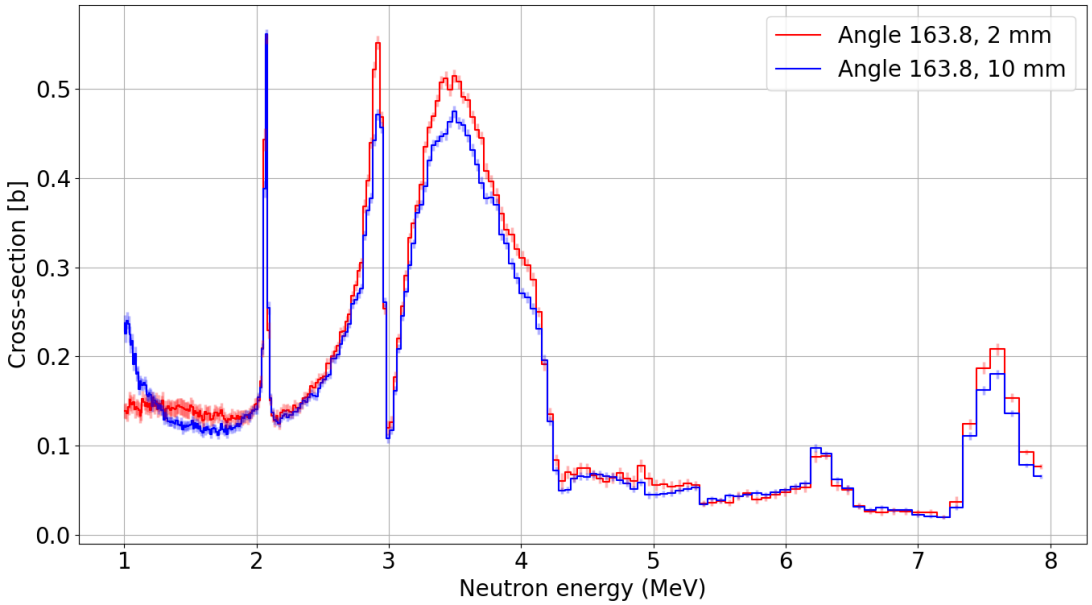

Figure 20: The experimental cross sections for the 2 mm and 10 mm target thicknesses with the correction factors implemented for the detector placed at 163.8°.

5 Discussion

This research aims to develop a method that effectively removes the multiple neutron scattering effects from neutron scattering cross section measurements on a 2 mm and 10 mm thick carbon target. In this chapter, the methods and obtained results are discussed. Also, this chapter discusses if the aim of the research is fulfilled and what could be improved in the future.

5.1 Physics lists

The usage of the correct physics lists has shown to be the most crucial aspect for this research. This becomes apparent when the comparison between the different physics lists are analysed. The Gluon Quark String model and the Fritiof Parton model have shown to have negligible impact for modelling the multiple scattering behaviour of neutrons in a carbon target. This is in accordance with the literature presented in the Methods chapter. These physics lists use calculations and databases for neutron energies exceeding 15 and 5 GeV, respectively. Moreover, for the Binary Cascade model and the Bertini Intranuclear Cascade model, no clear improvement in modelling the multiple neutron scattering is obtained. This is to be expected, since the models are similar in modelling and calculations methodology, both working for neutron energies lower than 10 GeV. After incorporating the High Precision neutron model to any of the previously mentioned physics lists combination, a multiple scattering result that can be validated through literature review as correct, was obtained. This showcases the importance of validating neutron data through comparison between separate physics lists combinations.

5.2 Neutron Detection Acceptance

The first key finding from this research is the significant improvement in neutron detection acceptance with the newly designed detector setup in Geant4. The ring-shaped detector configuration resulted in an average improvement of 700% in neutron detection yield compared to the experimental setup, for the 2 mm and 10 mm thick target. The result is expected, as the effective detector area surrounding the carbon target is increased. Furthermore, this result suggests that the new configuration is less computationally expensive, since more neutron scattering data can be obtained using the same amount of incident neutrons. An increased amount of data increases the overall reliability and accuracy of the measurements and a drastic decrease in computation times.

5.3 Multiple Scattering Percentages

The calculated multiple scattering percentages show an overall higher value for detector angles close to 90°, suggesting that neutrons that are captured by a detector close to 90° have scattered off more carbon nuclei than for detectors placed at other angles. This is in perfect alignment with the expectations, as the carbon target is disc-shaped and the has the most material in between the centre of the

target and any of the detectors, for detectors placed close to 90°. At 4.3 MeV neutron energy, the detector angles close to 163.8° show a drastic increase in multiple scattering for the 2 mm and 10 mm thick targets, which is 0.2 MeV lower than the experimental research suggests. This deviation might be due to the differences in target composition when comparing the experimental composition to the one used in this research, since ^{12}C and ^{13}C have different (in)elastic cross sections in the 1-8 MeV energy range, see the cross section plots for ^{12}C and ^{13}C from the ENDF-V.III database in Chapter 7.2.

5.4 Corrected Neutron Cross Sections

The implementation of the multiple scattering correction factor on the experimental neutron scattering cross sections resulted in varying results. The detector angles 100.6°, 79.4° and 58.3° resulted in the cross sections for 2 mm and 10 mm target thickness deviating more from each other subsequent to correction, compared to before applying the corrections. It is remarkable, since the overall multiple scattering percentages for these detector angles are higher than for the other detector angles. This indicates that there is a missing component that is not incorporated in the correction factor that becomes apparent at higher multiple scattering percentages. The reasons for the deviations found in the results are discussed in the following sub-chapter.

5.5 Limitations and Future Research

In this research, the percentages of ^{12}C and ^{13}C inside the carbon target are based on the natural abundances of the materials on earth. However, the carbon target used in the experimental research might be different than the one used in this research. This is one of the possible causes of error in the calculations of the correction factors. For applications of correction factors from models to experimentally obtained data, as performed in this research, the target material composition and geometry should be determined with greater precision in order to allow accurate results to be obtained.

Furthermore, the number of data points in the 1-8 MeV neutron energy range was limited to the exact neutron energy range of the experimentally obtained cross sections, which is composed of 256 data points. The spread of the data points in the experimental data is uneven; towards a neutron energy of 1.00 MeV, there are more data points than towards a neutron energy 8.00 MeV. For increasing the accuracy of calculations on the corrected cross sections in further research, the number of data points on the measured energy spectrum should be increased drastically.

When examining the scintillation detector configuration of the ELISA setup at GELINA, it is found that the detector casings and other surrounding components are exposed to scattered neutrons propagating towards directions other than the detector itself. As a result, neutrons may scatter off one of the mentioned components and subsequently be detected by one of the detectors. In Geant4, this problem is not existing, since the detectors are defined as cylindrical or ring-shaped volumes. Any

neutron entering one of the volumes results in a neutron count and no surrounding components that may cause unwanted scattering events are present. For future research, the surrounding components of the ELISA setup, such as the detector casings should be added to the Geant4 simulation in order to account for unaccounted effects caused by their presence.

Finally, the beam profile of the neutron beam in Geant4 deviates from the beam profile of the experimental research. In the simulation, a needle-like beam profile is used for the neutron beam that collides with the carbon target. The beam profile used at the GELINA facility is wider instead of needle-like, which may cause deviations between data obtained through simulation and experiment.

6 Conclusion

A method consisting of implementing a correction factor that accounts for the multiple scattering occurring in a carbon target when exposed to a neutron beam of 1-8 MeV is successfully studied in this research. The method is developed using the Geant4 modelling software and is tested on experimental data from the ELISA setup at GELINA. Several physics lists, which determine the calculations in the modelling software, are tested throughout this study. It was found that no significant effects on using any combination of physics lists were found, except subsequent to incorporating the High Precision neutron model. Any combination of physics lists, with the addition of the High Precision neutron model, yielded similar results. The Fritiof Parton and the Binary Cascade models were used throughout the next steps of the study. Furthermore, an improved detector design for usage in the modelling software is proposed and tested. This resulted in an average increase in neutron detection yield of 700%. Overall, the multiple scattering percentages calculated at detector angles close to 90° were found to be higher than for other detector angles. This indicates that neutrons detected at angles close to 90° underwent more multiple scattering than at other angles. This is in accordance with previous studies and nuclear databases. Additionally, subsequent to implementation of the correction factor on the experimentally obtained neutron scattering cross sections, the method shows to negatively impact the cross sections measured close to detectors placed at 90°. Meaning that the cross sections measured for the 2 mm and 10 mm target deviated more subsequent to applying the correction than prior to applying the correction, for these angles close to 90°. For detector angles farther away from 90°, an improvement was found, ranging from 1.5% to 8.5%. Overall, the goal of achieving a deviation smaller than 5% is obtained for detectors placed at 121.7° and 37.2°.

Improvements could be made by ensuring closer resemblance of the target material composition (^{12}C and ^{13}C) for the experimental setup and the setup in Geant4. A similar procedure may be required for modelling the surrounding materials in Geant4, such as detector casings (with the correct material compositions and geometry). Also, smaller increments in the energy spectrum should be incorporated so that there is an increase in data points in the studied energy range. Finally, the needle-like beam profile for the neutron beam, used in Geant4, deviates from the beam profile from the experiment. This should be corrected in Geant4 in future experiments as the usage of a wider neutron beam profile results in different collision trajectories inside the carbon target, which eventually results in alterations in the correction factors.

Bibliography

[1] Pirovano, Elisa, "Neutron scattering cross section measurements with a new scintillator array," pp. IV, 166, 2017.

[2] M. Kerveno, A. Bacquias, C. Borcea, P. Dessagne, G. Henning, L. Mihailescu, A. Negret, M. Nyman, A. Olacel, A. Plompen, C. Rouki, G. Rudolf, and J. Thiry, "From gamma emissions to (n,xn) cross sections of interest: the role of gains and grapheme in nuclear reaction modeling," *EUROPEAN PHYSICAL JOURNAL A*, vol. 51, no. 167, pp. 1–18, 2015.

[3] M. Nyman, T. Adam, C. Borcea, M. Boromiza, P. Dessagne, G. Henning, M. Kerveno, A. Negret, A. Olacel, E. Pirovano, and A. Plompen, "New equipment for neutron scattering cross-section measurements at gelina," *EPJ Web Conf.*, vol. 239, p. 17003, 2020. [Online]. Available: https://doi.org/10.1051/epjconf/202023917003

[4] G. Lit, G. Bentoumit, Z. Tun, L. Li, and B. Sur, "Application of geant4 to the data analysis of thermal neutron scattering experiment," *Canadian Nuclear Laboratories*, 2024.

[5] F. Zhang, Z. Guifeng, Y. Zou, R. Yan, and H. Xu, "Core nuclear design and heat transfer analysis of a megawatt-level sic coated particle based vehicular micro reactor," *Nuclear Engineering and Design*, vol. 2023, p. 112668, 12 2023.

[6] M. Boromiza, C. Borcea, P. Dessagne, D. Ghita, T. Glodariu, G. Henning, M. Kerveno, N. Marginean, C. Mihai, R. Mihai, A. Negret, C. Nita, M. Nyman, A. Olacel, A. Oprea, A. J. M. Plompen, C. Sotty, G. Suliman, R. Suvaila, L. Stan, A. Turturica, and G. Turturica, "Nucleon inelastic scattering cross sections on ^{16}O and ^{28}Si," *Phys. Rev. C*, vol. 101, p. 024604, Feb 2020.

[7] *"Neutron/gamma psd liquid scintillator EJ-301, EJ-309"*, EljenTechnology. [Online]. Available: https://eljentechnology.com/images/products/data_sheets/EJ-301_EJ-309.pdf

[8] *"Neutron/gamma psd liquid scintillator EJ-301, EJ-309"*, Eljen Technology. [Online]. Available: https://eljentechnology.com/images/products/data_sheets/EJ-301_EJ-309.pdf

[9] D. Brown, M. Chadwick, R. Capote *et al.*, "ENDF/B-VIII.0: The 8^{th} major release of the nuclear reaction data library with CIELO-project cross sections, new standards and thermal scattering data," *Nuclear Data Sheets*, vol. 148, pp. 1 – 142, 2018, special Issue on Nuclear Reaction Data. [Online]. Available: https://www.sciencedirect.com/science/article/pii/S0090375218300206

[10] J. Allison *et al.*, "Recent developments in geant4," *Nuclear Instruments and Methods in Physics Research Section A: Accelerators, Spectrometers, Detectors and Associated Equipment*, vol. 835, pp. 186–225, 2016. [Online]. Available: https://www.sciencedirect.com/science/article/pii/S0168900216306957

[11] T. Wagner, C. R. Magill, and J. O. Herrle, *Carbon Isotopes*. Cham: Springer International Publishing, 2018, pp. 194–204. [Online]. Available: https://doi.org/10.1007/978-3-319-39312-4_176

[12] B. Andersson, G. Gustafson, and H. Pi, "The fritiof model for very high energy hadronic collisions," *Zeitschrift für Physik C Particles and Fields*, vol. 57, pp. 485–494, 09 1993.

[13] A. B. Kaidalov and K. A. Ter-Martirosian, "Multiple Production of Hadrons at High-Energies in the Model of Quark-Gluon Strings," *Sov. J. Nucl. Phys.*, vol. 39, p. 979, 1984.

[14] G. Folger, V. Ivanchenko, and J. Wellisch, "The binary cascade: Nucleon nuclear reactions," *The European Physical Journal A - Hadrons and Nuclei*, vol. 21, pp. 407–417, 09 2004.

[15] A. Heikkinen, N. Stepanov, and J. P. Wellisch, "Bertini intra-nuclear cascade implementation in geant4," 2003.

[16] D. Brown, M. Chadwick, R. Capote, A. Kahler, A. Trkov, and M. H. et al., "Endf/b-viii.0: The 8th major release of the nuclear reaction data library with cielo-project cross sections, new standards and thermal scattering data," *Nuclear Data Sheets*, vol. 148, pp. 1–142, 2018, special Issue on Nuclear Reaction Data. [Online]. Available: https://www.sciencedirect.com/science/article/pii/S0090375218300206

[17] G. Gkatis, E. Pirovanu, M. Diakaki, G. Noguere, M. Nyman, A. Oprea, C. Paradela, and A. J. M. Plompen, "Angular distribution measurements of neutron elastic scattering on natural carbon," pp. 1–12, 2024.

7 Appendix

7.1 Detector angles

Polar angles	16.2°	37.2°	58.3°	79.4°	100.6°	121.7°	142.8°	163.8°
Azimuthal angles	-90°	-30°	30°	90°				

Table 2: List of azimuthal and polar angles. The 32 detectors are placed at combinations between all these 12 angles.

7.2 Scattering cross sections ENDF/B-VIII.0

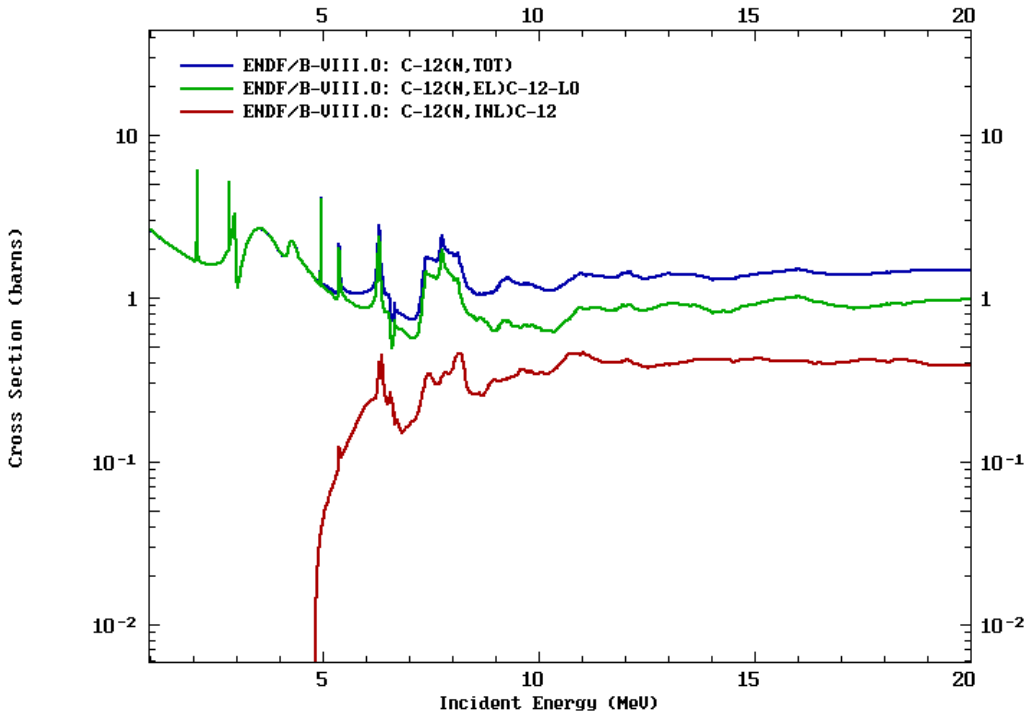

Figure 21: Cross sections of elastic scattering (green), inelastic scattering (red) and the total (blue) for the fast-neutron energy range for ^{12}C. The data is from the ENDF/B-VIII.0 database [9].

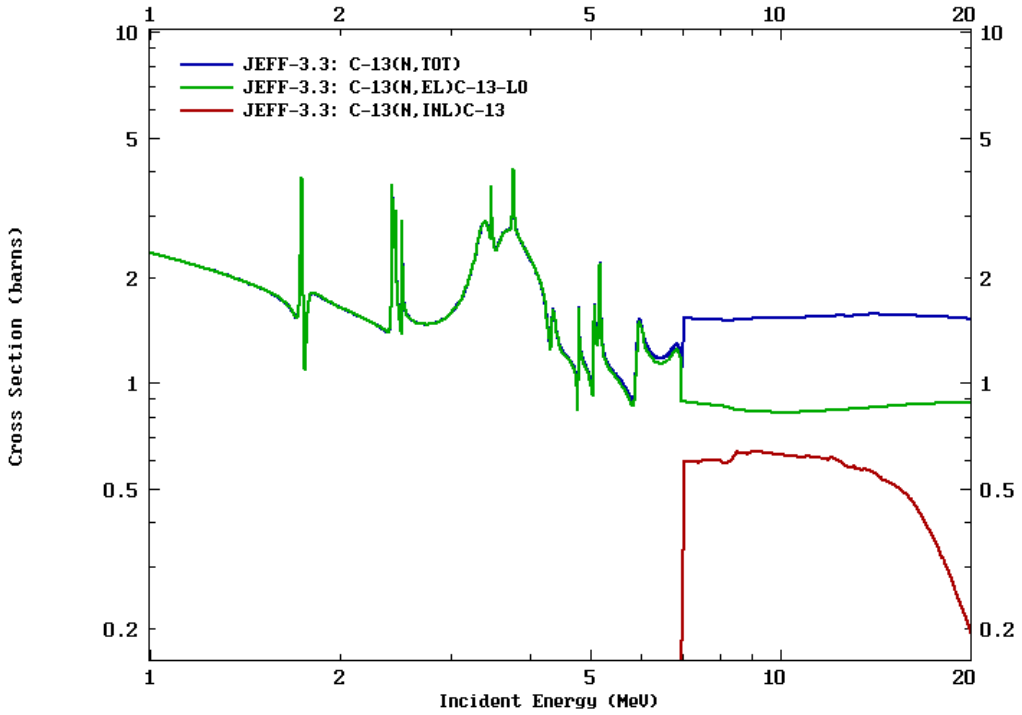

Figure 22: Cross sections of elastic scattering (green), inelastic scattering (red) and the total (blue) for the fast-neutron energy range for ^{13}C. The data is from the ENDF/B-VIII.0 database [9].

7.3 Derivations

7.3.1 Absolute error

$$\Delta f(a(b),b) = \sqrt{\left(\frac{\partial f}{\partial a}\right)^2 (\delta a)^2 + \left(\frac{\partial f}{\partial b}\right)^2 (\delta b)^2 + 2\left(\frac{\partial f}{\partial a}\right)\left(\frac{\partial f}{\partial b}\right) Cov(a,b)} \tag{14}$$

$$\Delta MSP = \sqrt{\left(\frac{\partial MSP}{\partial C_{>1}}\right)^2 (\delta C_{>1})^2 + \left(\frac{\partial MSP}{\partial C_T}\right)^2 (\delta C_T)^2 + 2\left(\frac{\partial MSP}{\partial C_{>1}}\right)\left(\frac{\partial MSP}{\partial C_T}\right) Cov(C_{>1},C_T)} \tag{15}$$

$$\frac{\partial MSP}{\partial C_{>1}} = \frac{100}{C_T} \tag{16}$$

$$\frac{\partial MSP}{\partial C_T} = -\frac{100 C_{>1}}{C_T} \tag{17}$$

$$Cov(C_{>1},C_T) = Var(C_{>1}) = C_{>1} \tag{18}$$

$$\Delta MSP = 100\sqrt{\frac{C_{>1}}{C_T^2} - \frac{C_{>1}^2}{C_T^3}} \tag{19}$$

7.3.2 Relative error

$$\frac{\Delta MSP}{|MSP|} = \frac{C_T}{C_{>1}}\sqrt{\frac{C_{>1}}{C_T^2} - \frac{C_{>1}^2}{C_T^3}} \tag{20}$$

$$\frac{\Delta MSP}{|MSP|} = \sqrt{\frac{C_T^2}{C_{>1}^2}\left(\frac{C_{>1}}{C_T^2} - \frac{C_{>1}^2}{C_T^3}\right)} \tag{21}$$

$$\frac{\Delta MSP}{|MSP|} = \sqrt{\frac{1}{C_{>1}} - \frac{1}{C_T}} \tag{22}$$

7.4 Physics lists plots

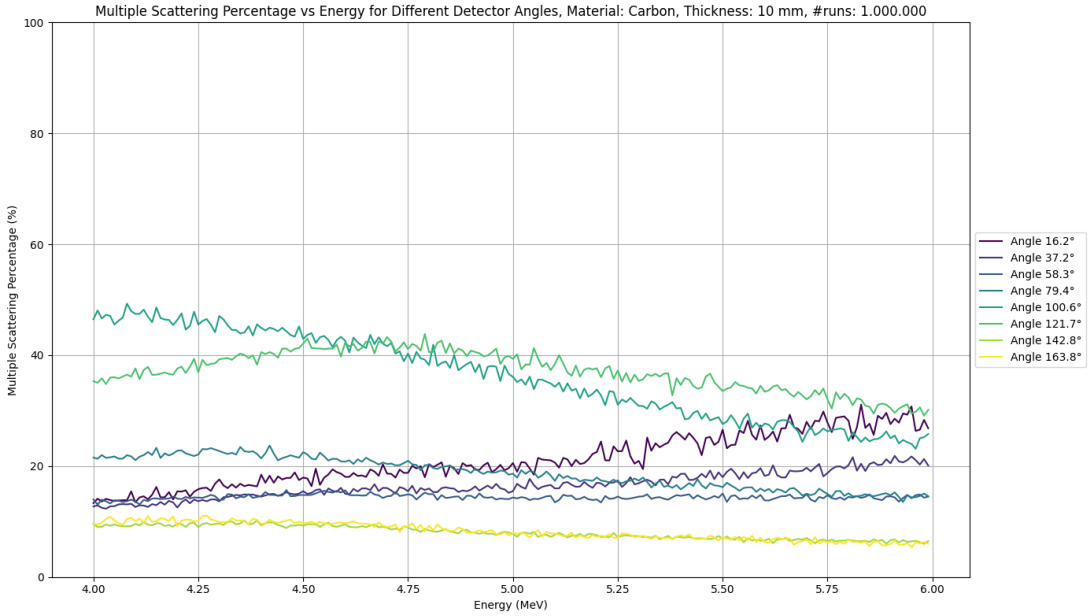

Figure 23: Multiple scattering percentage plot for 4-6 MeV, using the Fritiof Parton model and the Bertini Intranuclear model

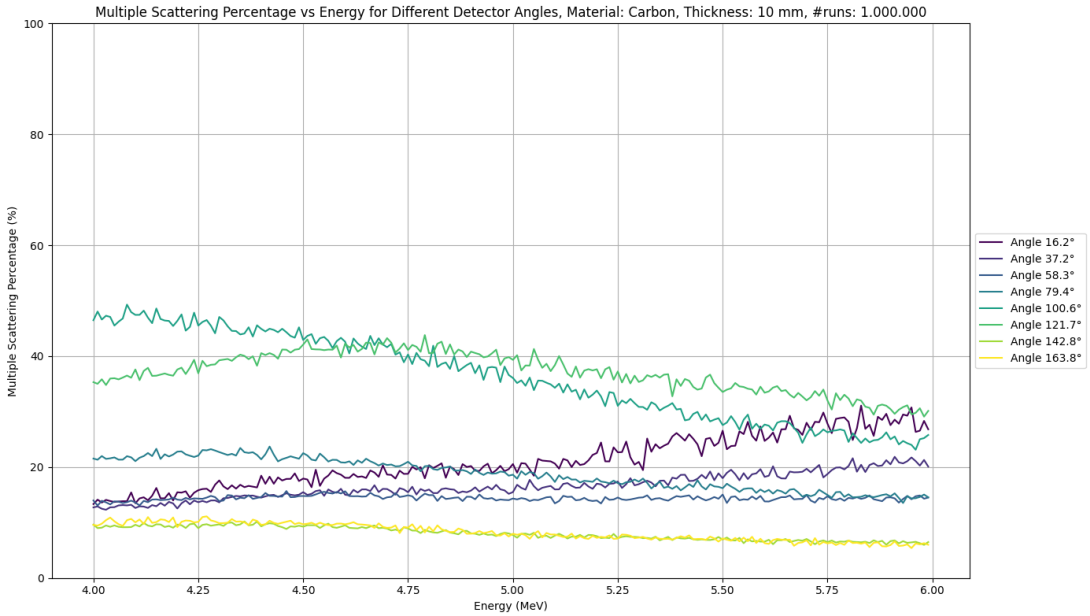

Figure 24: Multiple scattering percentage plot for 4-6 MeV, using the Fritiof Parton model and the Binary Cascade model

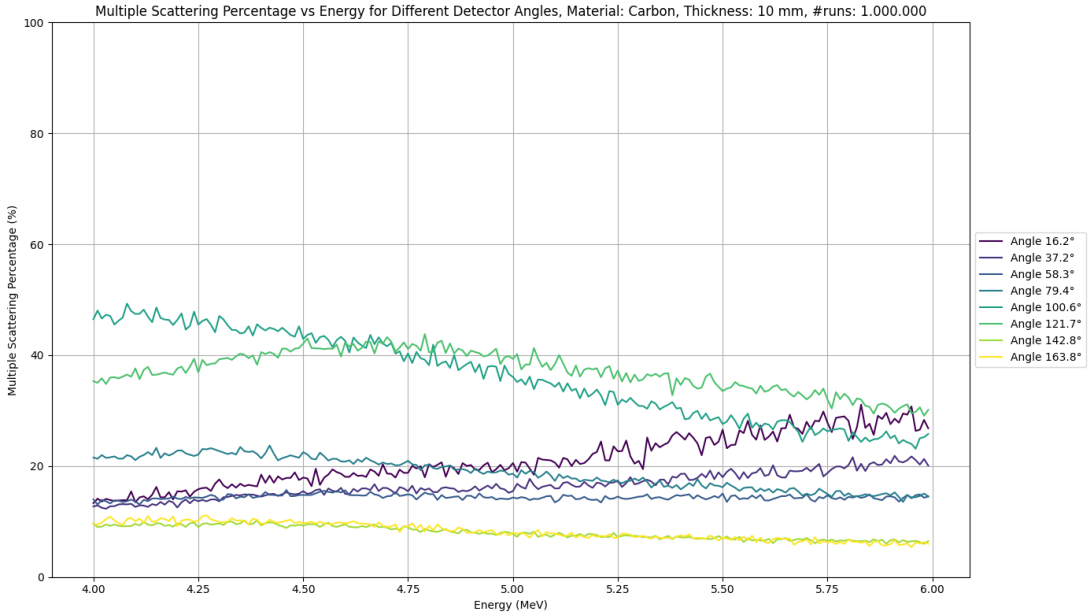

Figure 25: Multiple scattering percentage plot for 4-6 MeV, using the Quark-Gluon String model and the Bertini Intranuclear model

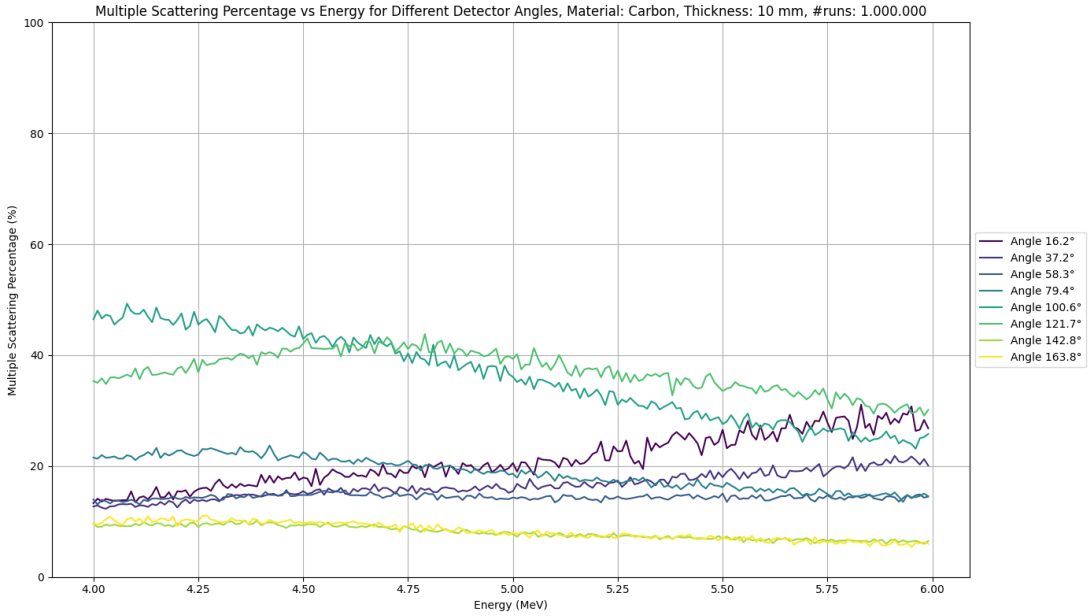

Figure 26: Multiple scattering percentage plot for 4-6 MeV, using the Quark-Gluon String model and the Binary Cascade model